



Synthesis of Nb₂O₅ nanoparticles through the oxidant peroxide method applied to organic pollutant photodegradation: A mechanistic study

Osmundo F. Lopes ^{a,b}, Elaine C. Paris ^b, Cauê Ribeiro ^{b,*}

^a Departamento de Química - UFSCar, Rod. Washington Luiz, km 235, CEP: 13565-905 São Carlos, SP, Brazil

^b Embrapa Instrumentação, Rua XV de Novembro, 1452, CEP: 13560-970, SP, Brazil

ARTICLE INFO

Article history:

Received 1 June 2013

Received in revised form 6 August 2013

Accepted 16 August 2013

Available online 28 August 2013

Keywords:

Niobium pentoxide

Nanoparticles

Photocatalysis

Photodegradation mechanism

Water treatment

ABSTRACT

This paper evaluates the influence of the hydrothermal treatment temperature on the phase formation, structure and photocatalytic potential of Nb₂O₅ nanoparticles obtained by the oxidant-peroxy method (OPM). The materials were characterized by X-ray diffraction (XRD), Raman spectroscopy, UV-vis diffuse reflectance spectroscopy (DRS), scanning and transmission electron microscopy (SEM and TEM), thermogravimetry (TGA), Fourier transform infrared spectrometry (FTIR) and N₂ adsorption isotherms. The photocatalytic efficiency of the Nb₂O₅ nanoparticles and the mechanism of degradation were evaluated with respect to the degradation of the contaminants: rhodamine B (RhB) and atrazine under UV and visible radiation. The synthesized nanoparticles presented mixed phases of Nb₂O₅ orthorhombic and Nb₂O₅·nH₂O, with particle size ranging from 30 to 40 nm and specific surface area ranging from 129 to 199 m²/g. The results showed that the nanoparticles can be applied as catalysts for photoactivated reactions. The rate constant of RhB photodegradation in the reaction catalyzed by the Nb₂O₅ samples was approximately 5 times higher than the rate observed for RhB direct photolysis (RhB self-photolysis), and approximately 2 times higher than RhB photodegradation catalyzed by TiO₂ (reference). The surface hydroxylation and crystallinity were the most important parameters for the photoactivity per unit area of the Nb₂O₅ nanoparticles obtained at lower (100 and 125 °C) and higher (150 and 175 °C) hydrothermal temperatures, respectively. Furthermore, under UV radiation, the main photodegradation mechanism occurred by the attack of ·OH radicals on the molecules (RhB and atrazine) and not by the direct oxidation of adsorbed molecules on the photocatalyst surface. Dye-sensitized photocatalysis was the main mechanism for RhB degradation under visible radiation.

© 2013 Elsevier B.V. All rights reserved.

1. Introduction

Niobium pentoxide (Nb₂O₅) is a promising material for application in many fields due its properties, such as high specific surface area [1], high selectivity [2,3] and strength of surface acid sites [4,5]. It has been largely studied as a catalyst in several types of reactions including dehydration [6–8], hydration [9], esterification [10,11], hydrolysis [1], condensation [12], alkylation [13,14], dehydrogenation [15], and in many types of oxidation reactions [2,16]. Furthermore, Nb₂O₅ presents a band gap ranging from 3.1 to 4.0 eV and high absorption in the light spectrum [5,17–19]. These properties indicate the potential application of this material in photocatalysis, such as in advanced oxidative processes

(AOPs) for the degradation of organic contaminants. Several studies have shown that Nb₂O₅ presents photocatalytic properties, such as selective oxidation of organic contaminants [2,18,20], photodegradation of organic dyes [17,21] and hydrogen production [19].

However, studies employing Nb₂O₅ as a photocatalyst generally apply this material in the micrometric form, obtained by the simple calcination of commercial oxide or through treatment with reactants such as hydrogen peroxide, acids and bases [17,19,20]. This is a drawback for heterogeneous catalysis because it is a surface phenomenon that is strongly dependent on the catalyst surface area and adsorbed surface groups, such as OH⁻, and is therefore dependent on the catalyst particle size. Despite the technological importance of nanoparticulated Nb₂O₅ [22], few preparation methods have been reported in the literature because Nb⁵⁺ ions are very unstable in aqueous solution [23–25]. Soft-chemistry methods may be suitable for the production of controlled surface areas and thus, the oxidant-peroxy method (OPM), through hydrothermal treatment, is a promising alternative because it is performed at low temperatures (100–200 °C). Because hydrothermal annealing

* Corresponding author. Tel.: +55 16 2107 2915; fax: +55 16 2107 2902.

E-mail addresses: osmundo.iq@hotmail.com (O.F. Lopes), elaine.paris@embrapa.br (E.C. Paris), caue.ribeiro@embrapa.br, caue1977@gmail.com (C. Ribeiro).

allows the crystallization process to occur in mild conditions, this does not eliminate the hydroxyl groups in as-formed surfaces, which results in a material with high surface area and consequently greater number of acid sites [26]. This synthesis was previously reported by Leite et al., who obtained, through the OPM method, a pseudo-hexagonal Nb_2O_5 phase with different morphologies, presenting high surface areas and a large number of acid sites [22]. However, the potential of this route to produce Nb_2O_5 as an active photocatalyst was not properly investigated.

Therefore, the aim of this paper was to evaluate the photocatalytic potential of niobium oxide nanoparticles produced by the OPM method and to describe the dependence of the phase and structure on the hydrothermal treatment temperature and time. To study the photoactivity and the active mechanisms involved in the produced materials, rhodamine B (dye) and atrazine (pesticide) photodegradation under UV and visible radiation were used as probes, and a methodology for the detection of active oxidative species was investigated.

2. Materials and methods

2.1. Synthesis of Nb_2O_5

Nb_2O_5 nanoparticles were synthesized based on the procedure previously reported by Leite et al. [22]. Syntheses were performed by the OPM method using hydrothermal treatment for crystallization of the nanoparticles. The precursor ammonium niobium oxalate ($\text{NH}_4[\text{NbO}(\text{C}_2\text{O}_4)_2(\text{H}_2\text{O})_2]_n\text{H}_2\text{O}$ – CBMM, Brazil) was dissolved in 100 mL of distilled water under vigorous stirring, resulting in a transparent solution after 15 min. To this solution, hydrogen peroxide (Synth, 30% v/v) was added at a 10:1 $\text{H}_2\text{O}_2:\text{Nb}$ molar ratio, leading instantaneously to a transparent yellow solution, which indicates the formation of the niobium peroxy complex (NPC) [27]. NPC was crystallized by hydrothermal treatment, in a home-made stainless steel capsule with an internal covering of poly-tetrafluoroethylene, in which magnetic stirring could be applied to avoid agglomeration. The internal pressures were self-generated by water vapor pressure, according to the set temperature. The temperature of the hydrothermal treatment was studied by fixing the treatment time for 12 h and varying the temperature between 100, 125, 150 and 175 °C. These samples were identified as 100Nb12, 125Nb12, 150Nb12 and 175Nb12. The time of hydrothermal treatment was studied by fixing the treatment temperature at 125 °C and varying the time at 2, 12 and 24 h. These samples were identified such as 125Nb2, 125Nb12 and 125Nb24. After the specified reaction times, a white powder was formed in all cases. The powder was washed three times with distilled water and separated by centrifugation.

The hydrothermal treatment conditions, such as time and temperature, and the Nb precursor used in the synthesis have a strong effect on the final material properties, such as phase, morphology, particle size, and specific surface area and consequently, on the photocatalytic properties. In this way, niobium chloride (NbCl_5) was evaluated as a precursor to the Nb_2O_5 synthesis, to verify the effect of different Nb sources on the final material. Nb_2O_5 nanoparticles were synthesized based on the procedure previously reported method from Uekawa et al. [23]. NbCl_5 was fully dissolved in ethanol at a proportion of 50% weight. This solution was added to an NH_3 aqueous solution, leading to a final concentration of 0.5 mol L^{-1} . This procedure leads to a white precipitate of $\text{Nb}_2\text{O}_5 \cdot \text{nH}_2\text{O}$, which was washed repeatedly and separated by centrifugation. The precipitate was submitted to the same conditions for hydrothermal treatment, maintaining the molar ratio of $\text{Nb}^{5+}:\text{H}_2\text{O}_2$ at 1:10, and treating the material at 175 °C for 12 h. However, in this synthesis, the phase did not change from the $\text{Nb}_2\text{O}_5 \cdot \text{nH}_2\text{O}$ precursor, even at 175 °C/12 h (as observed in the

supplementary XRD data, Fig. 1S), which was sufficient for the crystallization of the material produced using the ammonium niobium oxalate.

2.2. Powder characterization

X-ray powder diffraction was conducted in a Shimadzu XRD 6000 at 30 kV and 30 mA with $\text{Cu K}\alpha$ radiation. In the analysis, the 2θ range from 10 to 70° in a step-scanning mode was used with a step width of 0.02° and a fixed time of 4 s. The Raman spectroscopy analyses were performed in a Horiba Jobin-Yvon Raman spectrometer coupled to an Olympus TM BX41 microscope, which was used either for focusing the laser to the desired point of the sample or for gathering the scattered radiation. All spectra were gathered with the use of a 514.5 nm argon laser. Ultraviolet-visible (UV-vis) absorption was recorded using a Cary 5G spectrometer in total reflection mode with an integration cell.

A field emission gun-scanning electron microscope (FEG-SEM JEOL JSM 6701F) operating at 5.0 kV was used to verify the material morphology. High resolution transmission electron microscopy (HRTEM TECNAL F50) operating at 200 kV was used to verify the crystallographic orientations. TEM samples were prepared by wetting carbon-coated copper grids with a drop of the colloidal suspensions and drying in air.

The Fourier transform infrared spectra (FTIR) were collected in a PerkinElmer Spectrum 1000. These analyses were performed to detect the presence of species such as, OH groups and adsorbed water on the surface of the synthesized samples. For this analysis, the samples were first kept at a constant temperature of 100 °C for 12 h and were then placed in a desiccator to ensure the same atmospheric conditions for all samples prior to FTIR analysis. The analysis of N_2 adsorption at 77 K was conducted in a Micrometrics ASAP 2000, and the specific surface area was obtained by the application of BET modeling. Before the analyses were performed, the samples were pre-treated (degassing) by heating at 80 °C under vacuum until reaching a degassing pressure of less than $10 \mu\text{m Hg}$.

Thermal degradation was evaluated using a TA Q500 thermogravimetric analyzer (TA Instruments, New Castle, DE, USA) under the following conditions: weight $10.00 \pm 0.50 \text{ mg}$; synthetic air flow 60 mL/min ; heating rate $100^\circ\text{C}/\text{min}$; and temperature range $100\text{--}900^\circ\text{C}$.

2.3. Evaluation of photocatalytic activity

The photocatalytic potential of the synthesized samples was evaluated through the degradation of two different contaminants, rhodamine B dye (RhB) and atrazine. The photoactivities were studied under UV and visible radiation, to separate possible sensitization effects. These tests were performed in a thermostated photoreactor at 18 °C with a UVC radiation source (Lamps Phillips TUV, 15 W and maximum intensity at 254 nm) and a visible radiation source (Osram, maximum intensity at 440 nm).

To perform the photocatalytic tests, different samples with the same photocatalyst amount (150 mg L^{-1}) were prepared by dispersing 3 mg of photocatalyst in 20.0 mL of aqueous RhB (Aldrich, 5.0 mg L^{-1}) or atrazine (Merck, 10.0 mg L^{-1}). Because commercial TiO_2 (Aldrich nanopowder, 99.7%) is referred to in several papers as the most widely used photocatalyst [25], this material was tested under the same conditions as the reference. At regular time intervals, the samples were collected and analyzed in a UV-vis spectrophotometer (Shimadzu-1601PC) in the absorbance mode monitor the degradation kinetics at 554 nm and 222 nm for RhB and atrazine, respectively. The samples in dye or in pesticide solution were kept in the dark for approximately 12 h before the photocatalytic tests to evaluate possible adsorption effects were performed. None of the samples showed significant adsorption.

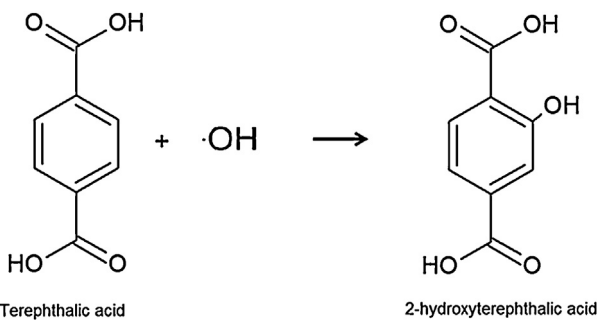


Fig. 1. Reaction between terephthalic acid and a hydroxyl radical, forming 2-hydroxyterephthalic acid.

The hydroxyl radical formation rate was determined according to the method proposed in a previous study [28], to evaluate the influence of this mechanism on contaminant degradation. This detection was performed indirectly, through the detection of 2-hydroxyterephthalic acid formed by the reaction of hydroxyl radicals with terephthalic acid (TPA – Aldrich, 98% purity). This reaction is described in Fig. 1, and the product can be detected by fluorescence techniques. For this procedure, a TPA solution (5.10^{-4} mol L $^{-1}$) was prepared in aqueous NaOH (2.10^{-3} mol L $^{-1}$). Multiple samples with the same photocatalyst amount (150 m L $^{-1}$) were prepared by dispersing 3 mg of photocatalyst in 20.0 mL of aqueous TPA. These tests were performed in a thermostated photoreactor at 20 °C with a UVC radiation source. The 2-hydroxyterephthalic acid concentration was monitored by fluorescence measurements in a PerkinElmer LS 50B fluorescence spectrometer. The fluorescence emission spectrum was obtained with 315 nm excitation, and the solution was measured at 30, 60, 120 and 240 min. The 2-hydroxyterephthalic acid presents a fluorescence intensity at approximately 425 nm. The peak attributed to 2-hydroxyterephthalic acid is proportional to the concentration of ·OH radicals. Therefore, the behavior of the fluorescence intensity against illumination time is linear, and the slope is proportional to the kinetics constants of the ·OH radical formation.

3. Results and discussion

3.1. Nb_2O_5 characterization

The structural and phase formation analysis of the Nb_2O_5 samples in a medium and the long-range order in the crystalline lattice

were evaluated by X-ray diffraction (XRD). Fig. 2a shows the XRD patterns of the samples as a function of the hydrothermal treatment temperature. The pattern resembles the orthorhombic Nb_2O_5 phase according to the Joint Committee on Powder Diffraction Standards (JCPDS) number 28-0317. Analysis of this figure indicated that an increase in the synthesis temperature led to more crystalline materials. The broad peaks are relative to the hydrated niobium oxide because the appearance of the peak in the XRD at $2\theta \approx 26^\circ$ is related to the intermediate conditions of crystallization for HNB_3O_8 [30], and the peak at $2\theta \approx 12^\circ$ is related to hydration water forming lamellae [31].

Fig. 2b shows the Raman spectra of the samples under hydrothermal treatment with temperature variation. The peak between 650 and 710 cm $^{-1}$ is assigned to the symmetric stretching mode of Nb–O polyhedra (NbO_6^{4-} , NbO_7^{4-} e NbO_8^{4-}) [32,33]. The broad shoulder at 960 cm $^{-1}$ is assigned to the stretching of the Nb=O surface groups. The peak intensity indicates the amorphous degree and the presence of acid groups in the sample [34,35]. The vibration mode at 215 cm $^{-1}$ is assigned to the stretching of the Nb–O–Nb bonds. 100Nb12 has a broad peak at 652 cm $^{-1}$, which is characteristic of hydrated niobium oxide ($\text{Nb}_2\text{O}_5 \cdot n\text{H}_2\text{O}$), and the poorly defined shoulder at 707 cm $^{-1}$ is characteristic of the orthorhombic phase. This indicates that the sample has a higher proportion of $\text{Nb}_2\text{O}_5 \cdot n\text{H}_2\text{O}$ than the orthorhombic phase. The increase in the synthesis temperature caused a decrease in the peak at 652 cm $^{-1}$ and an increase in the peak at 707 cm $^{-1}$. Therefore, the increase in the synthesis temperature increases the proportion of orthorhombic phase relative to $\text{Nb}_2\text{O}_5 \cdot n\text{H}_2\text{O}$ [29,32,34].

Fig. 2b shows that the increase of the synthesis temperature causes a decrease in the peak at 960 cm $^{-1}$. This indicates that the increase in the synthesis temperature decreased the amount of Nb=O and acid surface groups and increased the material crystallinity. In other words, materials synthesized at lower temperatures (100 °C) showed lower crystallinity and higher amounts of acid surface groups. In this way, an increase in the synthesis temperature led to sharp peak; this is related to the increase of the crystallinity, according to the values of the crystallite size that were estimated by the Scherrer equation (Table 1).

The band gap energies of the samples, obtained as a function of the hydrothermal temperature, were determined by UV-vis diffuse reflectance spectroscopy applying the Tauc model [36,37] according to the following equation:

$$\alpha h\nu = A(h\nu - E_g)^{n/2} \quad (1)$$

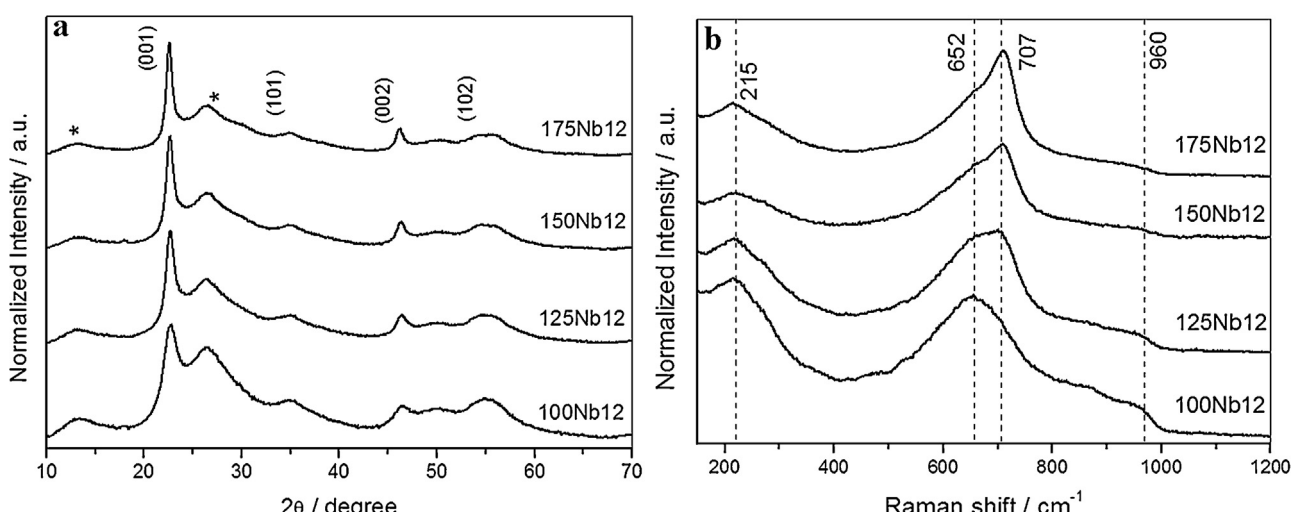


Fig. 2. X-ray diffraction patterns with crystallographic planes of the orthorhombic phase identified and $\text{Nb}_2\text{O}_5 \cdot n\text{H}_2\text{O}$ identified as (*) (a), and Raman spectra (b) of samples obtained from hydrothermal treatment with temperature variation.

Table 1

Crystallite size estimated by the Scherrer equation from the XRD data.

| 2θ/° | (h k l) | Crystallite size/nm | | | |
|-------|---------|---------------------|---------|---------|---------|
| | | 100Nb12 | 125Nb12 | 150Nb12 | 175Nb12 |
| 22.5 | (0 0 1) | 12.6 | 19.3 | 21.6 | 25.3 |
| 46.15 | (0 0 2) | 12.4 | 18.3 | 21.6 | 22.2 |

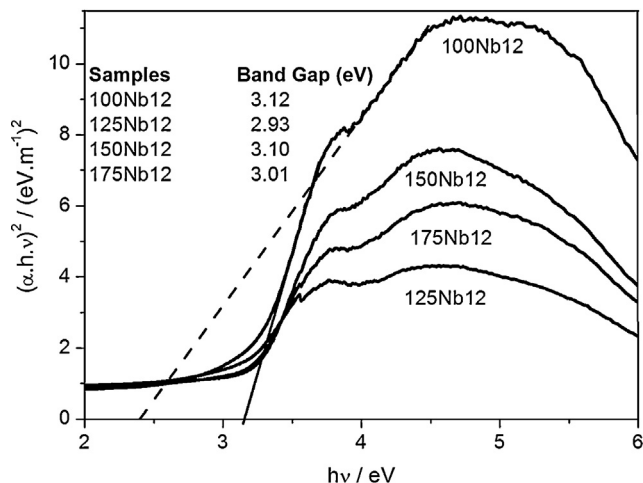


Fig. 3. (a) Plot of $\alpha(h\nu)^2$ against $h\nu$ from the UV-vis diffuse reflectance for samples obtained by hydrothermal treatment with temperature variation. In the inset, the band gap values are described. (b) Plot of $\alpha(h\nu)$ by $h\nu$ of the spectroscopic data shows the presence of two band gaps, evidenced by the dotted and straight lines.

where α , h , ν , E_g , and A are the absorption coefficient, Planck's constant, light frequency, band gap energy and a constant, respectively. Constant n is dependent on the type of transition between the semiconductor bands, where $n = 1$ for direct transition and $n = 4$ for indirect transition. The band gap value can be obtained from

the x-intercept of the tangent line in a plot of $(\alpha h\nu)^2$ versus energy $h\nu$, as in Fig. 3. The band gap values found in Fig. 3 for the synthesized samples had small changes between them, ranging from 2.9 to 3.1 eV. The presence of two distinct band gaps (represented by the two straight lines) is clearly observed. This confirms the coexistence of different phases (Nb_2O_5 and $\text{Nb}_2\text{O}_5 \cdot n\text{H}_2\text{O}$).

The samples obtained as a function of the hydrothermal treatment with time variation (125Nb2, 125Nb12 and 125Nb24) did not present significant differences in their properties, as observed by the XRD data (Fig. S2), which shows similar profiles and relative intensities. The crystallite sizes were estimated by the Scherrer equation and show similar sizes (Table S1). These samples have spherical morphology and a size of 30–35 nm, as observed in the SEM-FEG images (Fig. S3). Thus, because these materials present similar properties, they are expected to present similar photoactivity.

Fig. 4 shows the representative FEG-SEM images of the synthesized samples. Samples 100Nb12, 125Nb12 and 150Nb12 show spherical agglomerates forming units with an average size ranging from 31 to 35 nm. These samples present isotropic morphology, which indicates that the growth mechanism follows classical growth mechanisms. The 175Nb12 sample has two types of morphology, spherical and nano-needles with different lengths. These results suggest that the increase in the synthesis temperature led to significant modifications in the morphology.

Fig. 5 shows the representative HRTEM images for the 125Nb12 and 175Nb12 samples. The 125Nb12 sample (Fig. 5a) presents an interlayer distance of 1.13 nm, which is relative to the formation of stacked structures, such as lamellae. This interlayer distance is characteristic of the (0 0 2) plane of the HNb_3O_8 phase [39]. This sample has agglomerates composed of spherical nanocrystals with diameters ranging from 9 to 14 nm, as indicated by the white arrows according to crystallite size (Table 1), which also reveals an amorphous region.

The 125Nb12 sample presents small crystallites, indicating that this sample is in an intermediate state of crystallinity, as previously

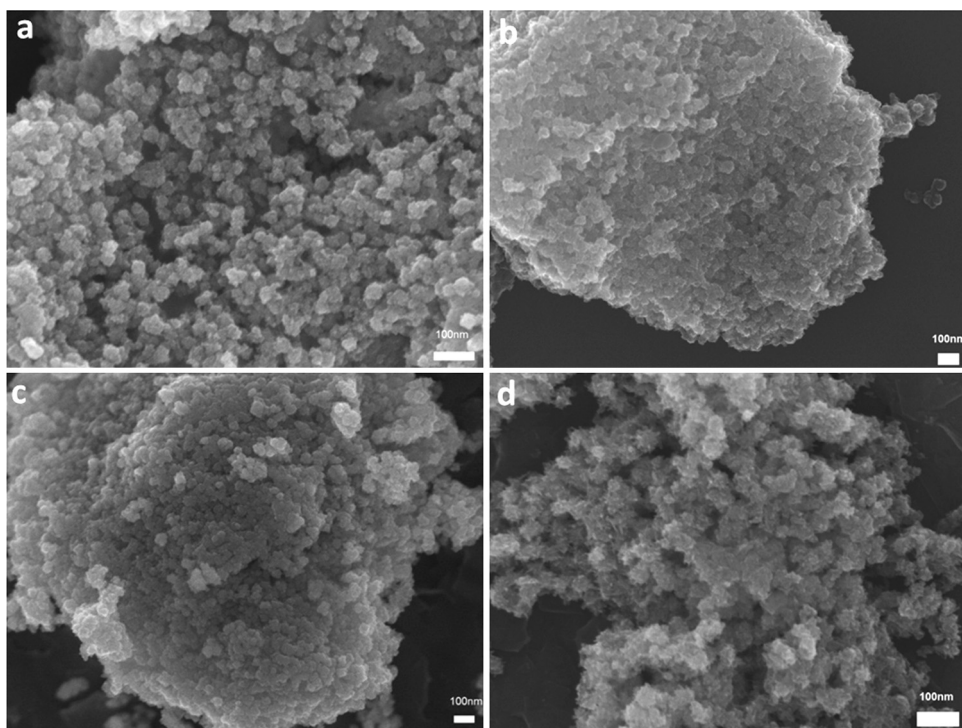


Fig. 4. Representative FEG-SEM images of the samples obtained by hydrothermal treatment with temperature variation: a) 100Nb12, b) 125Nb12, c) 150Nb12 and d) 175Nb12.

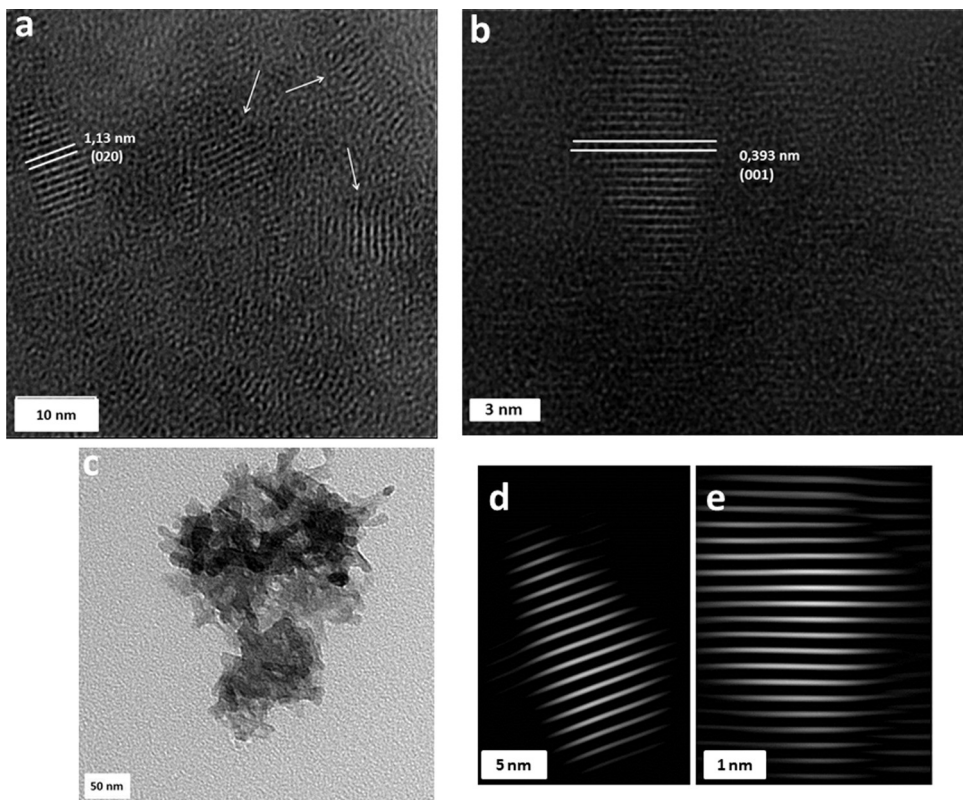


Fig. 5. TEM images of the synthesized samples a) 125Nb12 HRTEM, b) 175Nb12 HRTEM, c) 175Nb12 bright field image, d) FFT filtered image of 125Nb12 sample, e) FFT filtered image of 175Nb12 sample.

observed by XRD. This suggests that, at temperatures below 150 °C, the system does not have enough energy for long range crystallization. The spherical shape decreases the overall surface energy, and in these conditions, this morphology became preferential [40]. The 175Nb12 sample (Fig. 5b) has lattice parameters consistent with the plane (001) of the orthorhombic phase (0.393 nm). This sample has elongated nanorod-like nanocrystals of 50 nm length (Fig. 5c). The filtered images for 125Nb12 and 175Nb12 (Fig. 4d and e, respectively) were obtained by fast Fourier transform (FFT), in which the structural regularity of the crystallographic planes can be observed.

3.2. Photocatalytic properties

The photocatalytic efficiency of the samples obtained as a function of the hydrothermal temperature (100Nb12, 125Nb12, 150Nb12 and 175Nb12) was evaluated by photodegradation kinetics from the plot of dye or pesticide concentration as a function of exposure time under UV radiation (Fig. 6a and b, respectively). The direct photolysis was evaluated for RhB and atrazine solutions without any catalyst (RhB and atrazine self-photolysis). In this experiment, nearly 10% of the RhB was degraded after 3 h, and nearly 20% of the atrazine was degraded after 30 min, which is a reference for the catalyst effect. Commercial TiO₂ (Aldrich nanopowder, 99.7%) was used as a reference.

In both cases, the order of photoactivity showed the same trend, and all the synthesized Nb₂O₅ samples showed higher photoactivity than commercial TiO₂. Sample 125Nb12 was the most photoactive, followed by 100Nb12, 150Nb12 and 175Nb12. From the exponential profile observed in the photodegradation kinetics, and considering that the active sites have a constant number, the average number of active sites must be proportional to the surface

area [41,42]. The reaction is expected to follow first-order kinetics:

$$\nu = \frac{d[\text{Pollutant}]}{dt} = k[\text{Pollutant}] \quad (2)$$

where ν is the reaction rate, [Pollutant] is the dye or pesticide concentration, t is the reaction time, and k is the first-order rate constant. Integrating the rate law Eq. (2), it is possible to obtain:

$$\ln \frac{[\text{Pollutant}]}{[\text{Pollutant}]_0} = -kt \quad (3)$$

According to Eq. (3), the plot of $\ln([\text{Pollutant}]/[\text{Pollutant}]_0)$ versus t is a straight line with a slope equal to k . The first-order rate constants are shown in the Table 2, where R^2 values (higher than 0.99), confirm that the dye and pesticide photodegradation follows a first-order mechanism.

The photocatalytic efficiency of the samples obtained as a function of the hydrothermal time (125Nb2, 125Nb12 and 125Nb24) was evaluated by photodegradation kinetics from the plot of the dye concentration as a function of exposure time under UV radiation (Fig. S4). These samples showed similar photoactivity, as observed in Table S2, where all the samples presented almost

Table 2

First-order rate constants for the RhB and atrazine photodegradation tests performed under UV radiation.

| Samples | $k_{\text{RhB}} 10^{-3}/\text{min}^{-1}$ | $k_{\text{AT}} 10^{-2}/\text{min}^{-1}$ |
|------------------|--|---|
| Photolysis | 0.62 ± 0.25 | 1.12 |
| TiO ₂ | 1.66 ± 0.14 | 1.17 |
| 100Nb12 | 2.63 ± 0.15 | 2.65 |
| 125Nb12 | 3.23 ± 0.49 | 3.00 |
| 150Nb12 | 2.06 ± 0.23 | 2.20 |
| 175Nb12 | 1.83 ± 0.28 | 2.20 |

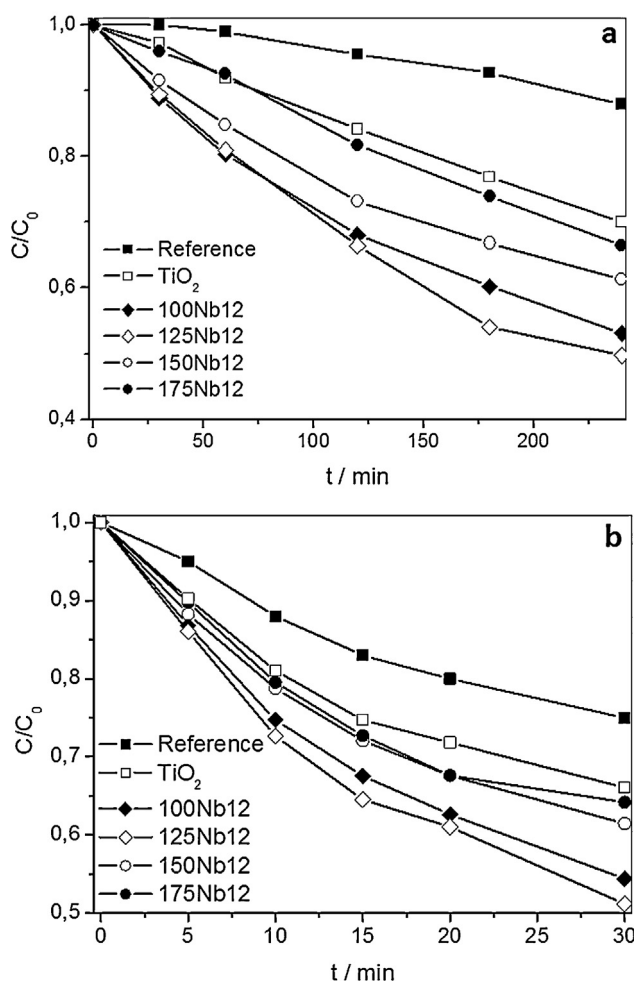


Fig. 6. Photodegradation kinetics determination from the plots of a) RhB and b) atrazine concentration as a function of exposure time under UV radiation (254 nm). In the inset, the degradation profile of a representative sample.

identical k values for rhodamine B photodegradation. The time of hydrothermal treatment did not significantly influence the properties of the obtained materials.

Assuming that the hydroxyl radical formation mechanism plays an important role in this photocatalytic process, the number of OH⁻ surface groups may have a strong effect on the photoactivity of the materials. The Fourier transform infrared spectroscopic data from 3800 to 2600 cm⁻¹ can be observed in Fig. 7. This region has two important bands, at 3400 and 3150 cm⁻¹, which were assigned to the stretching of adsorbed water and the Nb—OH bond (surface hydroxylation), respectively. Increasing the synthesis temperature causes a reduction in the amount of adsorbed water and surface hydroxylation, according to the Raman spectra, which show a decrease of acid groups with an increase in the synthesis temperature (Fig. 2b). This fact is in accordance with the higher photoactivity observed for the samples produced at lower hydrothermal temperatures (100Nb12 and 125Nb12).

The specific surface area (SSA) data for the synthesized samples obtained by the BET model can be observed in Table 3. The increase in synthesis temperature caused an increase in the specific surface area of the material up to a synthesis temperature of 150 °C. This behavior can be explained by the synthesis mechanism (Fig. 8): at lower temperatures (100 °C), nanocrystals embedded in an amorphous matrix are formed, as observed in step 1; increasing the synthesis temperature (step 2) causes a greater formation of nanocrystals and a higher migration from the amorphous region

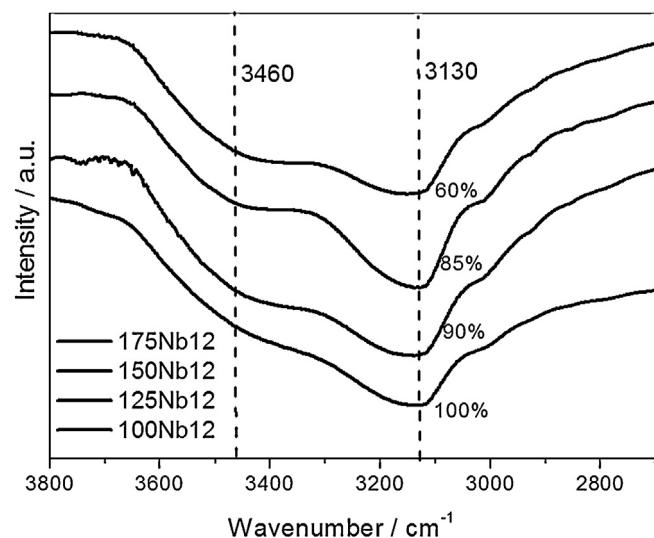


Fig. 7. FTIR spectra of the samples obtained by hydrothermal treatment with temperature variation.

occurs. Thus, the increase in temperature causes a disaggregation of the nanocrystals from the amorphous matrix, so the surface area is increased with the synthesis temperature. However, the synthesis performed at 175 °C shows a lower specific surface area than at 150 °C, which can be explained by step 3, where a greater amount of nanocrystals is formed. The formation of these nanocrystals at this temperature may subsequently lead to the oriented attachment growth mechanism, resulting in anisotropic crystals and reducing the total surface area.

TGA experiments were performed for the samples produced at 100 °C and 175 °C to verify the presence of volatile material from the precursors and the degradation of the structure. The TGA (and the derivative curve of TG and DTG) observed in Fig. S5 shows only a single mass loss mechanism, which is most likely associated with the dehydration of the structure. This is also shown in the DTG, where a single sharp peak is observed for the material produced at 175 °C, and a broader peak is observed for the material produced at 100 °C. The peaks are centered on the same temperature (245 °C), which can be correlated to the dehydration of the lamellar structure. The broadening observed in the material produced at lower temperature indicated the presence of some weakly bonded water, as expected. However, organic wastes were not observed in significant amounts, suggesting that this did not influence the specific surface area nor the material photoactivity.

3.3. Mechanism of photodegradation

There are two main mechanisms of photodegradation of organic compounds by photocatalytic processes: direct and indirect oxidation [43–45]. Direct oxidation occurs over the material surface, where the compound initially is adsorbed on the semiconductor surface, and when an electron-hole pair is formed by irradiation, the hole will migrate to the material surface, oxidizing the adsorbed

Table 3
Specific surface area of the synthesized samples and commercial TiO_2 .

| Samples | SSA/m ² /g |
|----------------|-----------------------|
| TiO_2 | 128 |
| 100Nb12 | 129 |
| 125Nb12 | 188 |
| 150Nb12 | 199 |
| 175Nb12 | 108 |

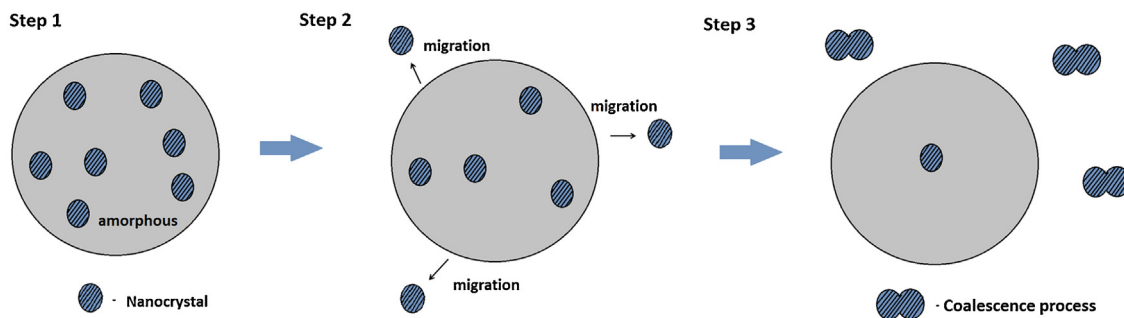


Fig. 8. Scheme of the Nb_2O_5 nanoparticle synthesis mechanism: crystallization (step 1), migration (step 2) and coalescence (step 3) processes.

compound [44,46,47]. In indirect oxidation, the electron–hole pair acts to form free radicals from surface groups, such as $\text{M}=\text{OH}$, O_2 , adsorbed water and others. The formed radical species are generally $\cdot\text{OH}$, HO_2^\bullet and $\text{O}_2^{\bullet-}$, which are able to oxidize organic compounds in solution [48,49]. Another photodegradation mechanism is sensitization, which occurs when an adsorbed molecule on the photocatalyst surface (photoactive under visible radiation) is excited from the ground state to the triplet excited state by visible radiation. This excited state is converted to a semi-oxidized radical cation by the injection of an electron into the conduction band of the photocatalyst [50]. This mechanism is particularly important in dyes that absorb in the visible range, and it is the basis of the design of dye-sensitized solar cells [51].

To identify the possible sensitization mechanism in the samples, the degradation of both contaminants was conducted under visible radiation, as shown in Fig. 9. Because the band gaps for the Nb_2O_5 samples were found in the 390 to 410 nm range, irradiation at 440 nm was not enough to generate electron–hole pairs. No photoactivity in atrazine degradation was found in the samples. This behavior was expected, because the wavelength that is necessary to excite atrazine is 222 nm, i.e., any electronic effect to this system is predictable. In contrast, the Nb_2O_5 samples showed significant photoactivity in RhB degradation, which absorbs at 554 nm. This fact indicates that during the RhB photodegradation under visible light, dye-sensitized photocatalysis plays a key role. When irradiated by visible light, RhB-homo ($+0.95 \text{ V vs NHE}$) is excited to RhB*-lumo (-1.42 V vs NHE) [52], and electrons are injected from RhB* lumo into the Nb_2O_5 conduction band (-0.9 V vs. NHE) [17,53]. This process occurs spontaneously, as observed in Fig. 10. In this way, the electrons in the Nb_2O_5 conduction band (-0.9 V vs.

NHE) reduce the O_2 surface-adsorbed into $\text{O}_2^{\bullet-}$ (-0.33 V vs. NHE) [54], which induces the formation of active oxidative species.

Because both mechanisms may be active in the degradation in UV irradiation, detection of hydroxyl radicals was performed to identify the relative importance of this mechanism. To detect the presence of the $\cdot\text{OH}$ radical, terephthalic acid was used as a fluorescent probe. The $\cdot\text{OH}$ radical is trapped by terephthalic acid to produce the fluorescent 2-hydroxyterephthalic acid (Fig. 1). The detection performed with the terephthalic acid method (Fig. 11) shows that all the samples produced hydroxyl radicals in substantial amounts. Additionally, the radical formation tendency was the same as observed in the photocatalytic results (Fig. 12), which indicates that the main mechanism for RhB and atrazine photodegradation occurs by hydroxyl radical attack.

The specific surface area of the materials in a catalytic process is of great importance because the increase in the specific surface area generates an increase in the number of active sites on the material surface, which consequently increases the kinetic rate of the process. Thus, the material photoactivity can be standardized by surface area to reveal the photoactivity associated solely with the material properties. A reliable approach is to divide the kinetics rate of the process by the surface area of each sample (Fig. 12).

Based on the photoactivity per unit area, the 100Nb12 sample was the most photoactive, followed by 125Nb12 \approx 175Nb12 and 150Nb12. The greater amount of the $\text{Nb}-\text{OH}$ surface groups and adsorbed water were determinant factors for the higher photoactivity. The 175Nb12 sample presents similar activity to the

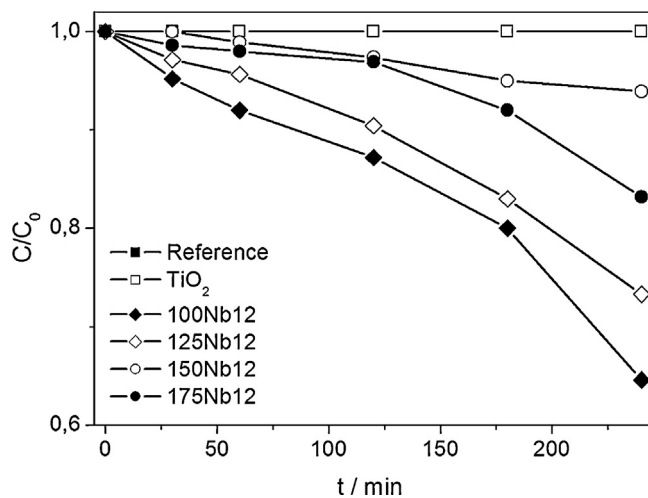


Fig. 9. Photodegradation kinetics determination from the plot of RhB concentration as a function of exposure time under visible radiation (440 nm).

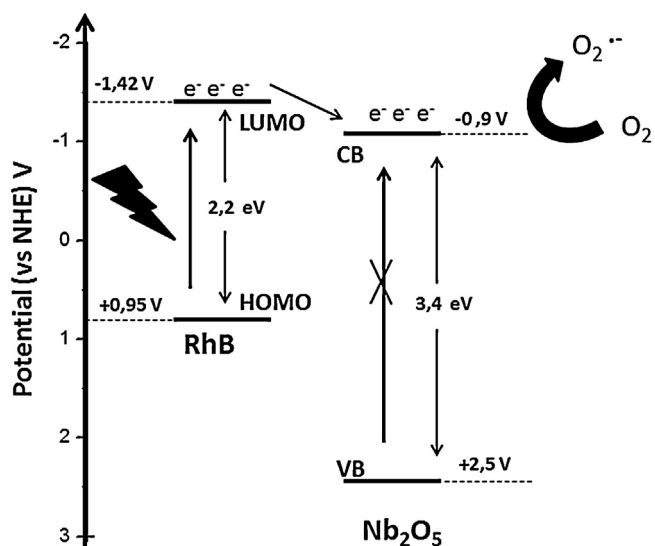


Fig. 10. The dye-sensitized photocatalysis mechanism: electron injection from the excited state of RhB, and the spontaneous formation of dye radical cations and superoxide radicals.

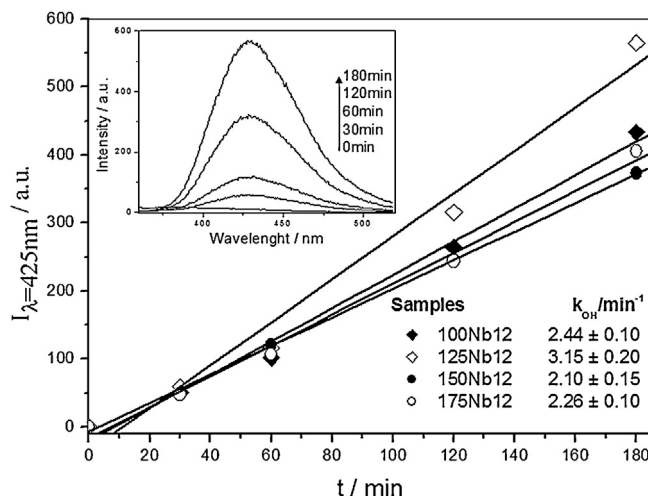


Fig. 11. Formation of hydroxyl radical by zero-order kinetics of the samples obtained by hydrothermal treatment with temperature variation. The spectra profile of 2-hydroxyterephthalic acid formation using representative samples, and the kinetics constant values for each sample can be observed in the inset.

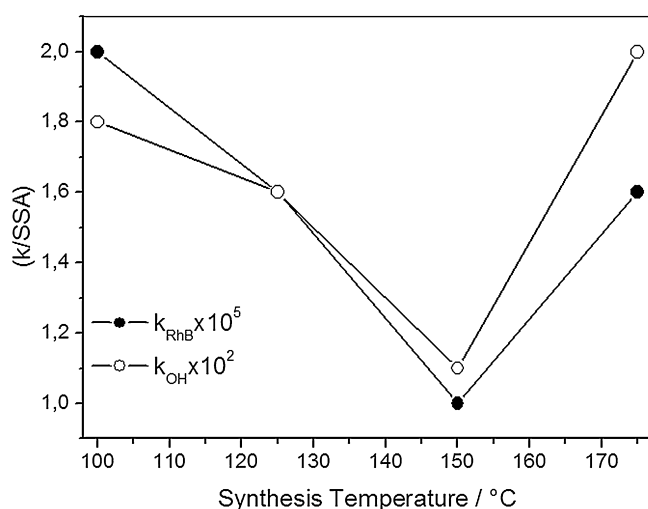


Fig. 12. Relationship between the kinetics rate constant and the $\cdot\text{OH}$ formation rate divided by the specific surface area and synthesis temperature.

125Nb12 and greater than 150Nb12, although the 175Nb12 sample has a lower number of surface groups. This behavior occurs because the 175Nb12 sample has a greater crystallinity degree and consequently a lower number of defects. These defects can act as recombination centers of electron–hole pairs, which decrease the photoactivity [41,51]. The lower amount of the surface groups in this sample was compensated by the higher crystallinity. A similar trend can be observed for $\cdot\text{OH}$ formation (Fig. 12), confirming that the main degradation mechanism occurs due to hydroxyl radical attack.

4. Conclusions

The results discussed in the present work indicate that Nb_2O_5 synthesized by the OPM method is a promising material for the photocatalysis of organic compounds degradation. The obtained materials presented a mixture of $\text{Nb}_2\text{O}_5 \cdot n\text{H}_2\text{O}$ and orthorhombic phases, with different morphologies and particle sizes ranging from 30 to 40 nm, high acidity and specific surface area (ranging from 129 to $199 \text{ m}^2/\text{g}$). Under UV radiation, the main degradation mechanism was the generation of hydroxyl radicals, which was demonstrated

to be effective for this reaction. The velocity constant of the RhB photodegradation reaction was approximately 5 times greater, when catalyzed by Nb_2O_5 samples, than for RhB direct photolysis (RhB self-photolysis), and approximately 2 times greater than RhB photodegradation when catalyzed by a TiO_2 reference. In addition, sensitized photocatalysis was shown to be an efficient method for the photoactive degradation of pollutants (as RhB) under visible light. For the synthesis performed at lower temperatures, surface hydroxylation was the most significant parameter of the photoactivity per unit area of material, whereas for the synthesis performed at higher temperatures, the crystallinity was the most influential parameter.

Acknowledgments

The authors thank FAPESP (project 2011/16546-7), CNPq, and FINEP for the financial support. We are also grateful to LCE DEMA and LIEC/UFSCar Brazil for providing HRTEM and Raman spectroscopy facilities, respectively.

Appendix A. Supplementary data

Supplementary data associated with this article can be found, in the online version, at <http://dx.doi.org/10.1016/j.apcatb.2013.08.031>.

References

- [1] K. Nakajima, T. Fukui, H. Kato, M. Kitano, J.N. Kondo, S. Hayashi, Chem. Mater. 22 (2010) 3332–3339.
- [2] S. Furukawa, Y. Ohno, T. Shishido, K. Teramura, T. Tanaka, J. Phys. Chem. C 117 (2013) 442–450.
- [3] S. Furukawa, Y. Ohno, T. Shishido, ACS Catal. 1 (2011) 1150–1153.
- [4] M. Ziolek, Catal. Today 78 (2003) 47–64.
- [5] I. Nowak, M. Ziolek, Chem. Rev. 99 (1999) 3603–3624.
- [6] P. Carniti, A. Gervasini, S. Biella, A. Auroux, Catal. Today 118 (2006) 373–378.
- [7] M. Marzo, A. Gervasini, P. Carniti, Catal. Today 192 (2012) 89–95.
- [8] V. Lebarbier, M. Houalla, T. Onfroy, Catal. Today 192 (2012) 123–129.
- [9] Y. Li, S. Yan, L. Qian, W. Yang, Z. Xie, Q. Chen, J. Catal. 241 (2006) 173–179.
- [10] V.S. Braga, I.C.L. Barros, F.A.C. Garcia, S.C.L. Dias, J.A. Dias, Catal. Today 133–135 (2008) 106–112.
- [11] I.A.L. Bassan, D.R. Nascimento, R.A.S. San Gil, M.I.P. da Silva, C.R. Moreira, W.A. Gonzalez, Fuel Process Technol. 106 (2013) 619–624.
- [12] M. Paulis, M. Martín, D.B. Soria, A. Díaz, J.A. Odriozola, M. Montes, Appl. Catal. A: Gen. 180 (1999) 411–420.
- [13] K. Yamashita, M. Hirano, K. Okumura, M. Niwa, Catal. Today 118 (2006) 385–391.
- [14] M.H.C. de la Cruz, M.A. Abdel-Rehim, A.S. Rocha, J.F.C. da Silva, A.C. Faro Jr., E.R. Lachter, Catal. Commun. 8 (2007) 1650–1654.
- [15] S. Chai, H. Wang, Y. Liang, B. Xu, J. Catal. 250 (2007) 342–349.
- [16] S. Furukawa, A. Tamura, T. Shishido, K. Teramura, T. Tanaka, Appl. Catal. B: Environ. 110 (2011) 216–220.
- [17] A.G.S. Prado, L.B. Bolzon, C.P. Pedroso, A.O. Moura, L.L. Costa, Appl. Catal. B: Environ. 82 (2008) 219–224.
- [18] T. Shishido, T. Miyatake, K. Teramura, Y. Hitomi, H. Yamashita, T. Tanaka, J. Phys. Chem. C 113 (2009) 18713–18718.
- [19] X. Chen, T. Yu, X. Fan, H. Zhang, Z. Li, J. Ye, et al., Appl. Surf. Sci. 253 (2007) 8500–8506.
- [20] T. Tanaka, H. Nojima, H. Yoshida, H. Nakagawa, T. Funabiki, S. Yoshida, Catal. Today 16 (1993) 297–307.
- [21] A.G.S. Prado, E.A. Faria, J.R. SouzaDe, J.D. Torres, J. Mol. Catal. A: Chem. 237 (2005) 115–119.
- [22] E.R. Leite, C.Vila, J. Bettini, E. Longo, J. Phys. Chem. B 110 (2006) 18088–18090.
- [23] N. Uekawa, T. Kudo, F. Mori, Y.J. Wu, K. Kakegawa, J. Colloids Interface Sci. 264 (2003) 378–384.
- [24] N. Pinna, M. Antonietti, M. Niederberger, Colloids Surf. A 250 (2004) 211–213.
- [25] M. Fox, M. Dulay, Chem. Rev. 93 (1993) 341–357.
- [26] F. Sayilan, S. Erdemoglu, M. Asilturk, M. Akarsu, S. Şener, H. Sayilan, Mater. Res. Bull. 41 (2006) 2276–2285.
- [27] Y. Narendar, G.L. Messing, Chem. Mater. 9 (1997) 580–587.
- [28] K. Ishibashi, A. Fujishima, T. Watanabe, K. Hashimoto, Electrochim. Commun. 2 (2000) 207–210.
- [29] E.I. Ko, J.G. Weissman, Catal. Today 8 (1990) 27–36.
- [30] X. Wang, G. Chen, C. Zhou, Y. Yu, G. Wang, Eur. J. Inorg. Chem. 2012 (2012) 1742–1749.
- [31] G.V. Tagliaferro, P.H.F. Pereira, L.A. Rodrigues, M.L.C.P. da Silva, Quim. Nova 34 (2011) 101–105.

- [32] J.M. Jehng, I.E. Wachs, *Chem. Mater.* 3 (1991) 100–107.
- [33] R. Brayner, F. Bozon-Verduraz, *Phys. Chem. Chem. Phys.* 5 (2003) 1457–1466.
- [34] S.M. Maurer, E.I. Ko, *J. Catal.* 135 (1992) 125–134.
- [35] S.K. Na Ayudhya, A. Soottitantawat, P. Prasertthdam, C. Satayaprasert, *Mater. Chem. Phys.* 110 (2008) 387–392.
- [36] J. Tauc, *Mater. Res. Bull.* 5 (1970) 721–730.
- [37] A.B. Murphy, *Sol. Energy Mater. Sol. Cells* 91 (2007) 1326–1337.
- [39] X. Li, W. Li, Z. Zhuang, Y. Zhong, Q. Li, L. Wang, *J. Phys. Chem. C* 116 (2012) 16047–16053.
- [40] Y. Zhao, C. Eley, J. Hu, J.S. Foord, L. Ye, H. He, *Angew. Chem. Int. Ed.* 51 (2012) 3846–3849.
- [41] V.R. de Mendonça, C. Ribeiro, *Appl. Catal. B: Environ.* 105 (2011) 298–305.
- [42] H.A.J.L. Mourão, A.R. Malagutti, C. Ribeiro, *Appl. Catal. A: Gen.* 382 (2010) 284–292.
- [43] K. Ishibashi, A. Fujishima, *J. Photochem. Photobiol. A* 134 (2000) 139–142.
- [44] Y. Mao, C. Schoeneich, K. Asmus, *J. Phys. Chem.* 95 (1991) 10080–10089.
- [45] M.A. Henderson, *Surf. Sci. Rep.* 66 (2011) 185–297.
- [46] E.R. Carraway, A.J. Hoffman, M.R. Hoffmann, *Environ. Sci. Technol.* 28 (1994) 786–793.
- [47] R. Andreozzi, V. Caprio, A. Insola, R. Marotta, *Catal. Today* 53 (1999) 51–59.
- [48] M.R. Hoffmann, S.T. Martin, W. Choi, D.W. Bahnemann, *Chem. Rev.* 95 (1995) 69–96.
- [49] K.Y. Jung, S. Bin Park, M. Anpo, *J. Photochem. Photobiol. A* 170 (2005) 247–252.
- [50] R. Vinu, S. Polisetti, G. Madras, *Chem. Eng. J.* 165 (2010) 784–797.
- [51] P. Chowdhury, J. Moreira, H. Gomaa, A.K. Ray, *Ind. Eng. Chem.* 51 (2012) 4523–4532.
- [52] L. Pan, J. Zou, S. Wang, Z.F. Huang, X. Zhang, L. Wang, *Appl. Surf. Sci.* 268 (2013) 252–258.
- [53] Y. Xu, M.A.A. Schoonen, *Am. Mineral.* 85 (2000) 543–556.
- [54] W.Y. Teoh, J.A. Scott, R. Amal, *J. Phys. Chem. Lett.* 3 (2012) 629–639.